Journal of Fluids and Structures (1998) **12,** 677–701
Article No. fl980168

COUPLED AND UNCOUPLED BENDING-TORSION RESPONSES OF TWIN-TAIL BUFFET

O. A. Kandil and E. F. Sheta

Aerospace Engineering Department, Old Dominion University, Norfolk, VA 23529, U.S.A.

(Received 31 August 1997 and in revised form 19 May 1998)

The effect of coupled and uncoupled bending and torsion modes on flexible twin-tail buffet is considered. This multidisciplinary problem is investigated using three sets of equations on a multi-block grid structure. The first set is the unsteady, compressible, laminar full Navier–Stokes equations which are used for obtaining the flow-filed vector and the aerodynamic loads on the twin tails. The second set is the coupled aeroelastic equations which are used for obtaining the bending and torsional deflections of the twin tails. The third set is the grid-displacement equations which are used for updating the grid coordinates due to the tail deflections. The configuration is pitched at 30° angle of attack and the free-stream Mach number and Reynolds number are 0·3 and 1·25 million, respectively. Keeping the twin tails as rigid surfaces, the problem is solved for the initial flow conditions. Next, the problem is solved for the flexible twin-tail responses due to the unsteady loads produced by the vortex breakdown flow of the delta-wing leading-edge vortex cores. The configuration is investigated for the effect of coupled and uncoupled bending and torsion modes, using two different separation distances of the twin-tail; the inboard and the outboard positions. The computational results are in good agreement with the experimental data.

1. INTRODUCTION

To maximize the effectiveness of fighter aircraft that operate well beyond the buffet onset boundary, the design of the new generation of fighter aircraft should account for both high maneuver capabilities and the aeroelastic buffet characteristics at high and wide range of angles of attack. The maneuver capabilities are achieved, for example in the F/A-18 fighter, through the combination of a leading-edge extension (LEX) with a delta wing, and the use of vertical tails. The LEX maintains lift at high angles of attack by generating a pair of vortices that trail aft, over the top of the aircraft. The vortex entrains air over the vertical tails to maintain stability of the aircraft. At some flight conditions, the vortices emanating from the highly swept LEX of the delta wing breakdown before reaching the vertical tails which get bathed in a wake of unsteady highly turbulent, swirling flow. The vortex-breakdown flow produces unsteady, unbalanced loads on the vertical tails and causes a peak in the pressure spectrum that may be tuned to different structural modes depending on the angle of attack and dynamic pressure. This in turn produces severe buffet on the tails and has led to their premature fatigue failure. If the power spectrum of the turbulence is accurately predicted, the intensity of the buffeting motion can be computed and the structural components of the aircraft can be designed accordingly.

Experimental investigation of the vertical tail buffet of the F/A-18 models have been conducted by several investigators, such as Sellers *et al.* (1988), Erickson *et al.* (1989), Wentz (1987), Lee & Brown (1990), and Cole *et al.* (1990). These experiments showed that the vortex produced by the LEX of the wing breaks down ahead of the vertical tails at angles of attack of 25° and higher, producing unsteady loads on the vertical tails; and the buffet response occurs in the first bending mode, increases with increasing dynamic pressure and is larger at $M = 0{\cdot}3$ than that at higher Mach numbers. Bean & Lee (1994) showed that buffeting in the torsional mode occurred at a lower angle of attack and at larger levels compared to the fundamental bending mode. An extensive experimental investigation has been conducted to study vortex–tail interaction on a 76° sharp-edged delta wing with vertical twin-tail configuration by Washburn, Jenkins & Ferman (1993). The vertical tails were placed at nine locations behind the wing. The experimental data showed that the aerodynamic loads are more sensitive to the chordwise tail location than its spanwise location. As the tails were moved laterally toward the vortex core, the buffeting response and excitation were reduced.

Kandil, Kandil & Massey (1993) presented the first successful computational simulation of the vertical tail buffet using a delta wing-single flexible vertical tail configuration. The tail was allowed to oscillate in bending modes. Unsteady breakdown of leading-edge vortex cores was captured, and unsteady pressure forces were obtained on the tail. Later on, Kandil *et al.* (1994, 1995) allowed the vertical tail to oscillate in both bending and torsional modes. The total deflections and frequencies of deflections and loads of the coupled bending-torsion case were found to be an order of magnitude higher than those of the bending case only. It has been shown that the tail oscillations change the vortex breakdown locations and the unsteady aerodynamic loads on the wing and tail.

The buffet responses of twin-tail model has been studied by Kandil, Sheta & Liu (1996). The twin tails were considered at $\alpha = 30°$ and for three different spanwise positions of the twin tails. A multi-block grid structure was used to solve the problem. The loads, deflections, frequencies and root bending moments were reduced as the twin tails moved laterally towards the vortex core. The outboard position of the tails produced the least of these responses. In a recent paper by Kandil, Sheta & Massey (1997), the buffet response of the twin-tail model in a turbulent flow was considered at a wide range of angles of attack. The computational results were in good quantitative agreement with the experimental data of Washburn *et al.* (1993).

In this paper, we consider the effect of coupled and uncoupled bending and torsion modes on the flexible twin-tail buffet response for two different spanwise separation distance of the twin-tail; the inboard position (33% wing span) and the outboard position (78% wing span). The computational results are compared with the experimental data of Washburn *et al.* (1993).

2. FORMULATION

The formulation consists of three sets of governing equations, along with certain initial and boundary conditions. The first set is the unsteady, compressible, laminar full Navier–Stokes equations. The second set consists of the aeroelastic equations for coupled bending and torsional modes. For uncoupled bending-torsion modes, the distance between the elastic axis and the inertial axis, x_θ, is set equals to zero in the aeroelastic equations. The third set consists of equations for deforming the grid according to the twin-tail deflections. Next, the governing equations of each set along with the initial and boundary conditions are given.

2.1. Fluid-Flow Equations

The conservative form of the dimensionless, unsteady, compressible, laminar full Navier–Stokes equations in terms of time-dependant, body-conformed coordinates

ξ^1, ξ^2 and ξ^3 is given by

$$\frac{\delta \bar{Q}}{\delta t} + \frac{\delta \bar{E}_m}{\delta \xi^m} - \frac{\delta (\bar{E}_v)_s}{\delta \xi^s} = 0; \quad m = 1 - 3, \quad s = 1 - 3, \tag{1}$$

where

$$\xi^m = \xi^m(x_1, x_2, x_3, t), \tag{2}$$

$$Q = \frac{1}{J}\,[\rho, \rho u_1, \rho u_2, \rho u_3, \rho e]^{\mathrm{T}}, \tag{3}$$

and $\bar{E}_m$ and $(\bar{E}_v)_s$ are the ξ^m-inviscid flux and ξ^s-viscous and heat conduction flux, respectively. Details of these fluxes are given by Kandil, Kandil & Massey (1993).

2.2. AEROELASTIC EQUATIONS

The dimensionless, linearized governing equations for the coupled bending and torsional vibrations of a vertical tail that is treated as a cantilevered beam are considered; see Kandil, Sheta & Massey (1997). The tail bending and torsional deflections occur about an elastic axis that is displaced from the inertial axis. These equations for the bending deflection, w, and the twist angle, θ, are given by

$$\frac{\partial^2}{\partial z^2}\left[EI(z)\frac{\partial^2 w}{\partial z^2}(z,t)\right] + m(z)\frac{\partial^2 w}{\partial t^2}(z,t) + m(z)\,x_\theta(z)\frac{\partial^2 \theta}{\partial t^2}(z,t) = N(z,t), \tag{4}$$

$$\frac{\partial}{\partial z}\left[GJ(z)\frac{\partial \theta}{\partial z}\right] - m(z)\,x_\theta\frac{\partial^2 w}{\partial t^2}(z,t) - I_\theta(z)\frac{\partial^2 \theta}{\partial t^2}(z,t) = -M_t(z,t), \tag{5}$$

where z is the vertical distance from the fixed support along the tail length, l_t, EI and GJ the bending and torsional stiffness of the tail section, m the mass per unit length, I_θ the mass-moment of inertia per unit length about the elastic axis, N the normal force per unit length, M_t the twisting moment per unit length and x_θ the distance between the elastic axis and the inertial axis. When $x_\theta = 0{\cdot}0$ the bending and torsion modes are dynamically decoupled. The characteristic parameters for the dimensionless equations are c^*, a^*_∞, ρ^*_∞ and c^*/a^*_∞, for the length, speed, density and time, where c^* is the delta wing root-chord length, a^*_∞ the free-stream speed of sound, and ρ^*_∞ the free-stream air density. The geometrical and natural boundary conditions on w and θ are given by

$$w(0,t) = \frac{\partial w}{\partial z}(0,t) = \frac{\partial^2 w}{\partial z^2}(l_t,t) = \frac{\partial}{\partial z}\left[EI(l_t)\frac{\partial^2 w}{\partial z^2}(l_t,t)\right] = 0, \tag{6}$$

$$\theta(0,t) = \frac{\partial \theta}{\partial z}(l_t,t) = 0. \tag{7}$$

The solution of equations (4) and (5) is given by

$$w(z,t) = \sum_{i=1}^{\hat{I}} \phi_i(z)\, q_i(t), \tag{8}$$

$$\theta(z,t) = \sum_{J=\hat{I}+1}^{M} \phi_j(z)\, q_j(t), \tag{9}$$

where ϕ_i and ϕ_j are comparison functions satisfying the free-vibration modes of bending and torsion, respectively, and q_i and q_j are generalized coordinates for bending and torsion, respectively. In this paper, the number of bending modes, $\hat{I}$, is six and the number of torsion modes, $M - \hat{I}$, is also six. Substituting equations (8) and (9) into equations (4) and (5) and using the Galerkin method along with integration by parts and the boundary conditions, equations (6) and (7), we get the following equation for the generalized coordinates q_i and q_j in matrix form:

$$\begin{bmatrix} M_{11} & M_{12} \\ M_{21} & M_{22} \end{bmatrix} \begin{Bmatrix} \ddot{q}_i \\ \ddot{q}_j \end{Bmatrix} + \begin{bmatrix} K_{11} & 0 \\ 0 & K_{22} \end{bmatrix} \begin{Bmatrix} q_i \\ q_j \end{Bmatrix} \begin{Bmatrix} \hat{N}_1 \\ \hat{N}_2 \end{Bmatrix}, \quad i = 1, 2, \ldots, \hat{I}, j = \hat{I} + 1, \ldots, M, \tag{10}$$

where the elements of the mass and stiffness matrices are

$$M_{11} = \int_0^{l_t} m\phi_r\phi_i \, \mathrm{d}z, \tag{11a}$$

$$M_{12} = M_{21} = \int_0^{l_t} m x_\theta \phi_r \phi_j \, \mathrm{d}z, \tag{11b}$$

$$M_{22} = \int_0^{l_t} I_\theta \phi_s \phi_j \, \mathrm{d}z, \tag{11c}$$

$$K_{11} = \int_0^{l_t} EI(\mathrm{d}^2\phi_r/\mathrm{d}z^2)(\mathrm{d}^2\phi_i/\mathrm{d}z^2) \, \mathrm{d}z, \tag{12a}$$

$$K_{22} = \int_0^{l_t} GJ(\mathrm{d}\phi_s/\mathrm{d}z)(\mathrm{d}\phi_j/\mathrm{d}z) \, \mathrm{d}z, \tag{12b}$$

$$\hat{N}_1 = \int_0^{l_t} \phi_r N \, \mathrm{d}z, \tag{13a}$$

$$\hat{N}_2 = \int_0^{l_t} \phi_s M_t \, \mathrm{d}z. \tag{13b}$$

The solution of equation (10), for q_i, $i = 1, 2, \ldots, \hat{I}$, and q_j, $j = \hat{I} + 1, \ldots, M$, is obtained using the four-stage Runge–Kutta scheme. Next, w, and θ are obtained from equations (8) and (9).

2.3. GRID DISPLACEMENT EQUATIONS

Once w and θ are obtained at the $n + 1$ time step, the new grid coordinates are obtained using interpolation equations. In these equations, the twin tail bending displacements, $w^{n+1}_{i,j,k}$, and their displacement through the torsion angle, $\theta^{n+1}_{i,j,k}$ are interpolated through cosine functions. The interpolation equations allow the grid points adjacent to the tail surfaces to move with the same deflections as those of the tails and keep the grid points at the computational boundaries fixed.

2.4. BOUNDARY AND INITIAL CONDITIONS

Boundary conditions consist of conditions for the fluid flow and conditions for the aeroelastic bending and torsional deflections of the twin tail. For the fluid flow, the

Riemann-invariant boundary conditions are enforced at the inflow and outflow boundaries of the computational domain. At the plane of geometric symmetry, periodic boundary conditions are specified. On the wing surface, the no-slip and no-penetration conditions are enforced and $\partial p/\partial n = 0$. On the tail surface, the no-slip and no-penetration conditions for the relative velocity components are enforced (points on the tail surface are moving). The normal pressure gradient is no longer equal to zero due to the acceleration of the grid points on the tail surface. This equation becomes $\partial p/\partial n = -\rho \mathbf{a}_t \cdot \hat{\mathbf{n}}$, where $\mathbf{a}_t$ is the acceleration of a point on the tail and $\hat{\mathbf{n}}$ is the unit normal.

The initial conditions of the fluid flow correspond to the free-stream conditions with no-slip and no-penetration conditions on the wing and tail. For the aeroelastic deflections of the tail, the initial conditions for any point on the tail are that the displacement and velocity are zero, $w(z, 0) = 0$, $\partial w(z, 0)/\partial t = 0$, $\theta(z, 0) = 0$ and $\partial \theta(z, 0)/\partial t = 0$.

3. METHOD OF SOLUTION

The first step is to solve for the fluid flow problem using the vortex-breakdown conditions and keeping the tail as a rigid beam. The Navier–Stokes equations are solved using the implicit, flux-difference splitting finite-volume scheme. The grid speed $\partial \xi^m/\partial t$ is set equal to zero in this step. This step provides the flow field solution along with the pressure differences across the tails. The results of this step are used as the initial conditions for the second step, where the tails are allowed to deflect by turning on equations (4) and (5). The pressure differences are used to generate the normal force and twisting moment per unit length of each tail. In the second step, the aeroelastic equations are used to obtain the twin tail deflections, $w_{i,j,k}$ and $\theta_{i,j,k}$. The grid displacement equations are then used to compute the new grid coordinates. The metric coefficient of the coordinate Jacobian matrix are updated as well as the grid speed, $\partial \xi^m/\partial t$. This computational cycle is repeated every time step.

4. COMPUTATIONAL APPLICATIONS AND DISCUSSION

4.1. Twin Tail-Delta Wing Configuration

The twin-tail-delta wing configuration consists of a 76°-swept back, sharp-edged delta wing (aspect ratio of one) and dynamically scaled flexible twin tails similar to those used by Washburn *et al.* (1993). The vertical tails are oriented normal to the upper surface of the delta wing and have a centreline sweep of 53·5°. A multi-block grid consisting of four blocks is used for the solution of the problem. The first block of a O-H grid for the wing and upstream region, with $101 \times 50 \times 54$ grid points in the wrap around, normal and axial directions, respectively. The second block is a H-H grid for the inboard region of the twin tails, with $23 \times 50 \times 13$ grid points in the wrap around, normal and axial directions, respectively. The third block is a H-H grid for the outboard region of the twin tails, with $79 \times 50 \times 13$ grid points in the wrap around, normal and axial directions, respectively. The fourth block is a O-H grid for the downstream region of the twin tails, with $101 \times 50 \times 25$ grid points in the wrap around, normal and axial directions, respectively. Figure 1 shows the three-dimensional grid topology and a front view blow-up of the twin tail-delta wing configuration.

Each tail is made of a single aluminium spar and Balsa wood covering. The aluminium spar has a taper ratio of 0·3 and a constant thickness of 0·001736. The chord length at the root is 0·03889 and at the tip is 0·011667, with a span length of 0·2223. The aluminium spar is constructed from 6061-T6 alloy with density, ρ, moduli of elasticity and rigidity, E and G,

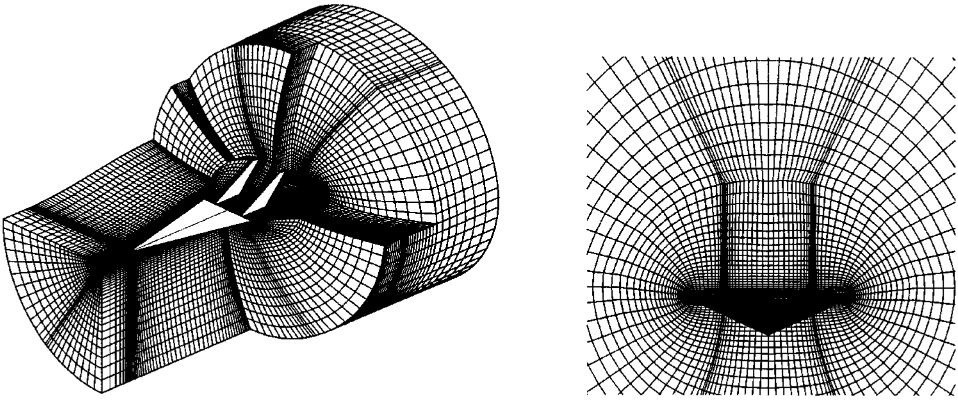

Figure 1. Three-dimensional grid topology and blow-up front view of the twin-tail-delta wing configuration (the tails are in midspan position).

of 2693 kg/m^3, $6{\cdot}896 \times 10^{10}$ N/m^2 and $2{\cdot}5925 \times 10^{10}$ N/m^2, respectively. The corresponding dimensionless quantities are 2198, $4{\cdot}595 \times 10^5$ and $1{\cdot}727 \times 10^5$, respectively.

The Balsa wood covering has a taper ratio of 0·23 and aspect ratio of 1·4. The chord length at the root is 0·2527 and at the tip is 0·058, with a span length of 0·2223. The Balsa thickness decreases gradually from 0·0211 at the tail root to 0·0111 at the tail midspan and then constant thickness of 0·0111 is maintained to the tail tip. The tail cross-section is a semi-diamond shape with a bevel angle of 20 °. The Balsa density, moduli of elasticity and rigidity, E and G, are 179·7 kg/m^3, $6{\cdot}896 \times 10^8$ N/m^2 and $2{\cdot}5925 \times 10^8$ N/m^2, respectively. The corresponding dimensionless quantities are 147, $4{\cdot}595 \times 10^3$ and $1{\cdot}727 \times 10^3$, respectively. The tails are assumed to be magnetically suspended and the leading edge of the tail root is positioned at $x/c = 1{\cdot}0$, measured from the wing apex. The configuration is pitched at 30 ° angle of attack and the free-stream Mach number and Reynolds number are 0·3 and $1{\cdot}25 \times 10^6$, respectively. The configuration is investigated for two spanwise positions of the twin tails; the inboard position and the outboard position corresponding to a separation distance between the twin tails of 33 and 78% of the wing span, respectively.

Keeping the twin tail as rigid surfaces, the unsteady laminar full Navier–Stokes equations are integrated time-accurately using the implicit, flux-difference splitting scheme of Roe with a Reynolds number, Re, of $1{\cdot}25 \times 10^6$ and an angle of attack of 30°. The initial conditions are obtained after 10 000 time steps with $\Delta t = 0{\cdot}001$. Next, the results of the coupled and uncoupled bending and torsion modes are presented. For the coupled bending and torsion case, the inertial axis is assumed downstream the elastic axis at $x_\theta = 0{\cdot}003$. For thet uncoupled case, x_θ is set equal to zero.

4.2. UNCOUPLED BENDING-TORSION MODES

Figures 2–7 show the results for the inboard position of the twin tail. Figure 2 shows three-dimensional views of the leading-edge vortex core particle traces and iso-total pressure surfaces. Figures 3 and 4 show front views of the total pressure contours on the wing surface and in cross-flow planes at $x = 1{\cdot}03$ and $x = 1{\cdot}22$,† and the instantaneous

---

† It is recalled that all lengths are nondimensionalized with respect to the delta wing root-chord length.

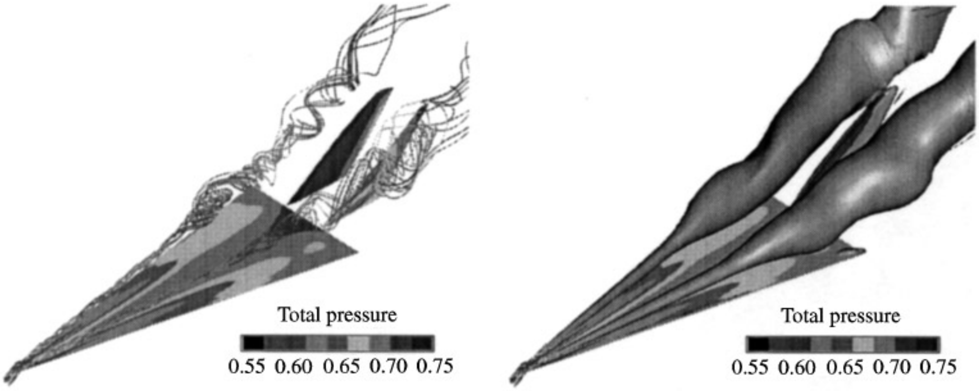

Figure 2. Three-dimensional views showing the total pressure on the surfaces, vortex core particle traces and iso-total pressure surfaces. Uncoupled case after $\tau = 9{\cdot}6$, Inboard position.

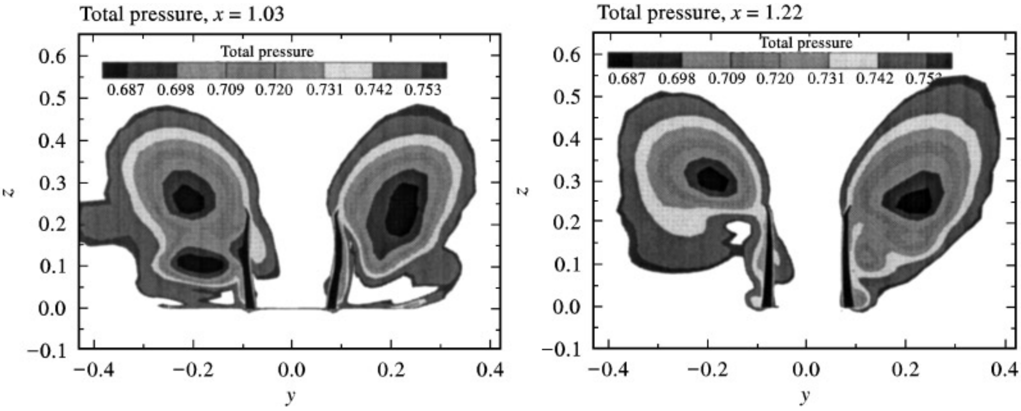

Figure 3. Snapshots of total pressure contours on cross-flow planes. Uncoupled case after $\tau = 9{\cdot}6$, inboard position.

streamlines in cross-flow planes at the same chord stations, respectively. The leading-edge vortex cores experience asymmetric breakdown upstream of the twin tail due to the upstream effect of the tails asymmetric motion. The vortices are totally outboard of the twin tail. The cores are moved upward as the flow travels downstream. Smaller size vortex cores appear underneath the primary wing vortex and they become larger in size as the flow travels downstream. These are the tail vortices observed by Washburn *et al.* (1993). The tail vortices exist at the outer surfaces of the tails and they are rotating in the opposite direction to those of the primary wing vortices.

Figure 5 shows the spanwise distribution of the surface-pressure coefficient after 9·6 dimensionless time units from the initial conditions, covering the wing from $x = 0{\cdot}3$ to $x = 1{\cdot}0$. The largest suction peaks are pronounced at the position of the wing vortex cores, and the peak values decrease as the flow travels down-stream. Low level suction peaks, corresponding to the secondary separation on the wing, are clearly observed next to the large level suction peaks.

Figure 6 shows the time history of bending and torsion deflections and load responses for the left and right tails for 20 dimensionless time units after the initial conditions. It is

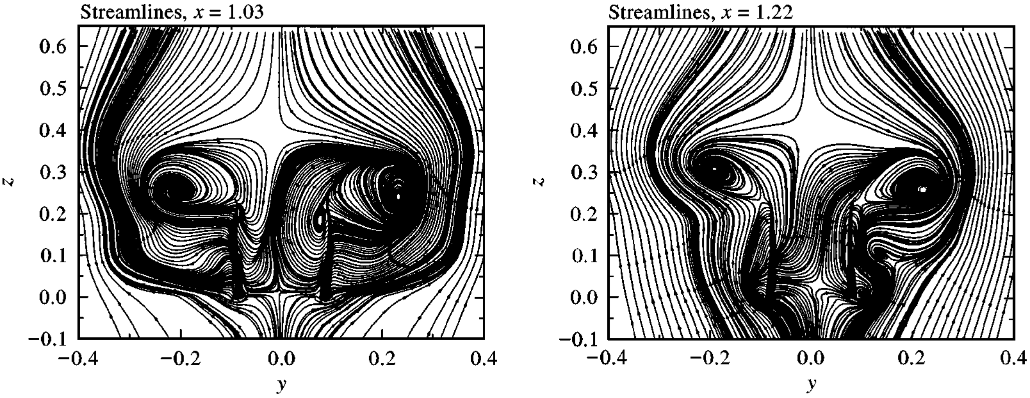

Figure 4. Snapshots of instantaneous streamlines on cross-flow planes. Uncoupled case after $\tau = 9{\cdot}6$, inboard position.

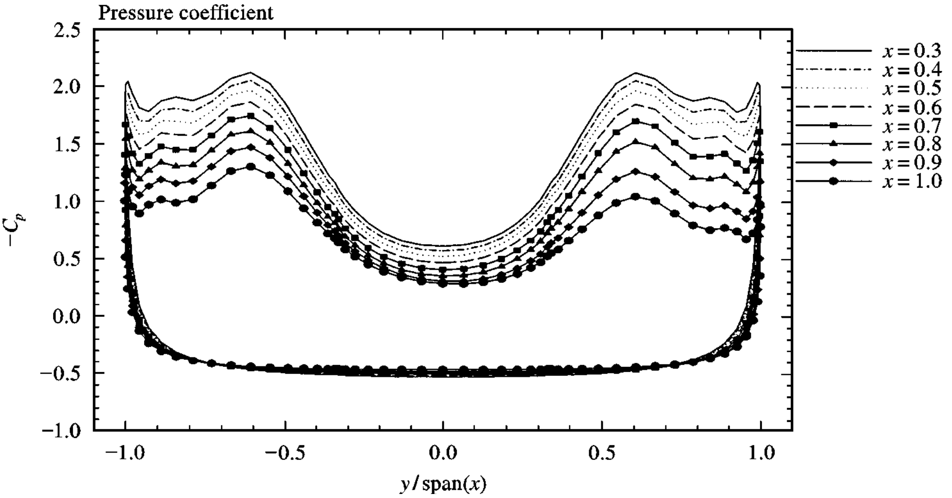

Figure 5. Distribution of pressure coefficient. Uncoupled case after $\tau = 9{\cdot}6$, Inboard position.

observed that the two tails deflect in an asymmetric manner. The frequencies of the torsion deflections are almost twice those of the bending deflections, while the frequencies of the normal loads are almost the same as those of the twisting moments. The normal forces are out of phase with the bending deflections, while the twisting moments are in phase with the torsion deflections.

Figure 7 shows the time history of the leading-edge total structural deflection and the root bending moment for the left and right tails for 20 dimensionless time units after the initial conditions. The tail deflections are in first-, second- and third-mode shapes. They are moving opposite to each other in an asymmetric manner.

Figures 8–13 show the results for the outboard position of the twin tail. Figure 8 shows three-dimensional views of the leading-edge vortex core particle traces and iso-total pressure surfaces. Figures 9 and 10 show front views of the total pressure contours on the wing surface and in cross-flow planes at $x = 1{\cdot}03$ and $x = 1{\cdot}22$, and the instantaneous streamlines

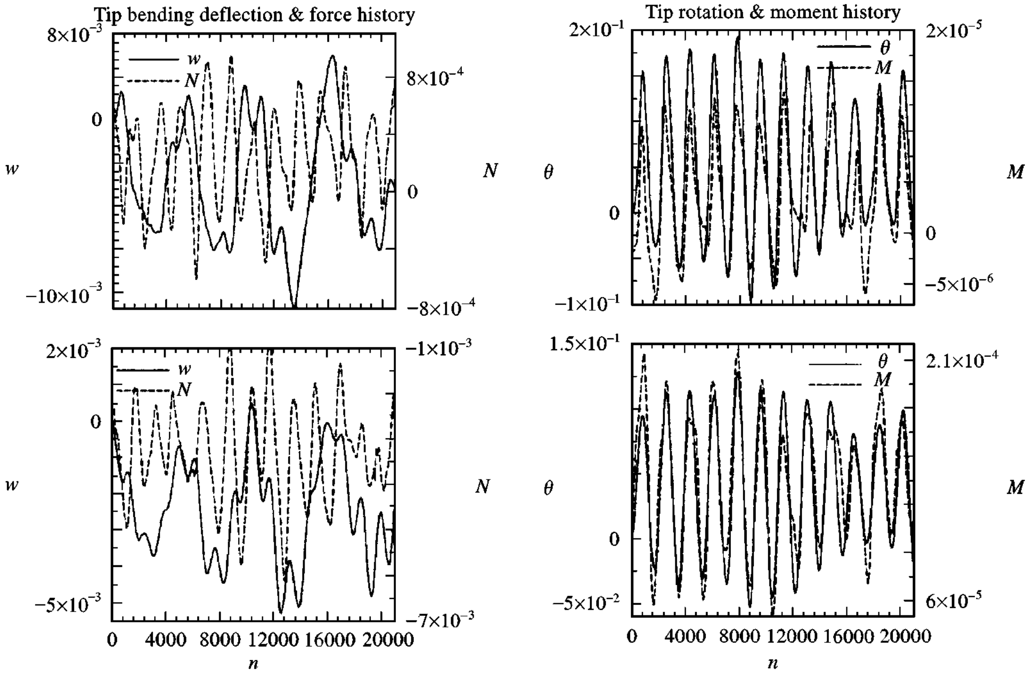

(a) Left tail

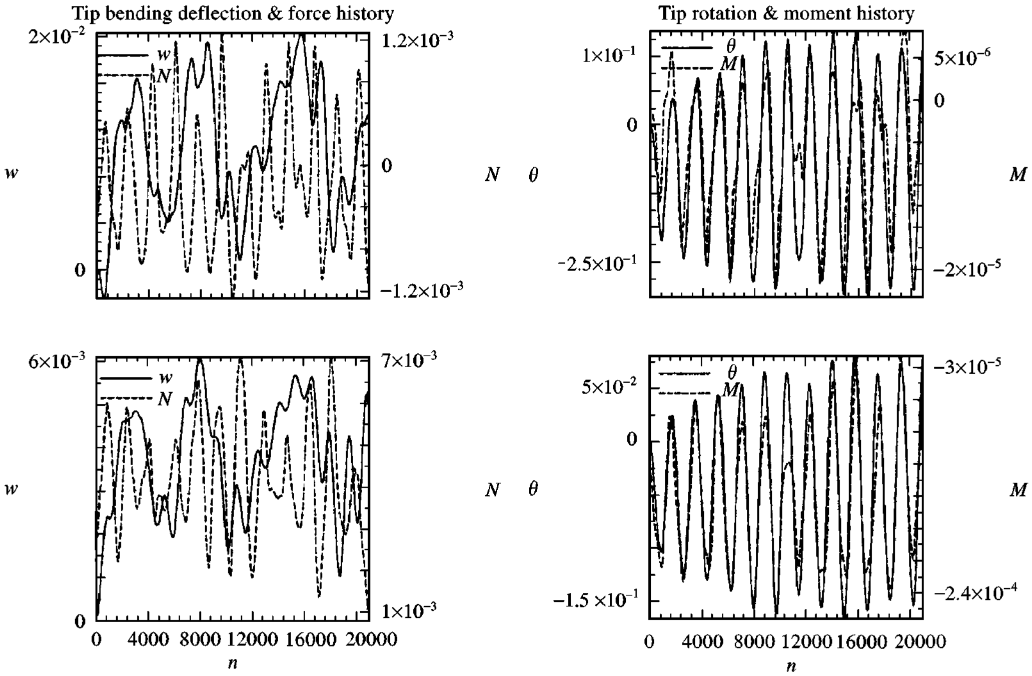

(b) Right tail

Figure 6. History of the deflection and load responses for an uncoupled bending-torsion case. $M_\infty = 0{\cdot}3$, $\alpha = 30^\circ$, $\mathrm{Re} = 1{\cdot}25 \times 10^6$, inboard position.

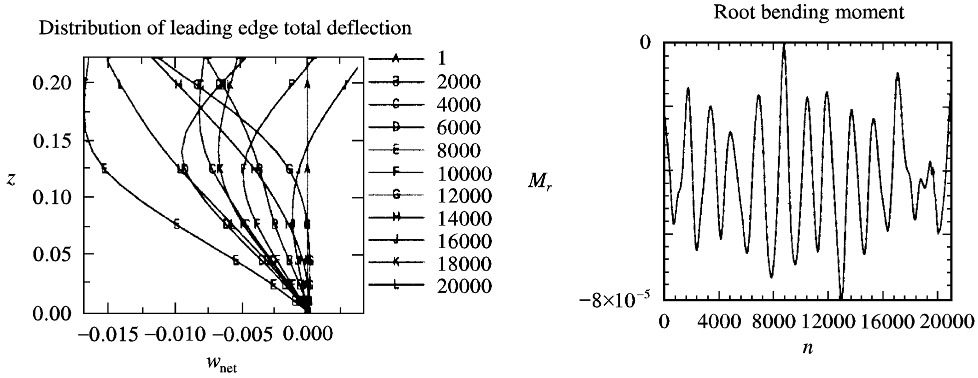

(a) Left tail

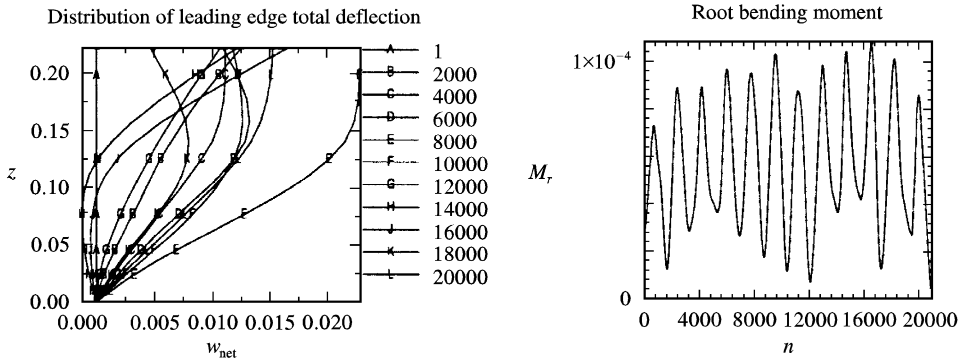

(b) Right tail

Figure 7. Tail leading-edge total structural deflections and root bending moment for an uncoupled bending-torsion case. $M_\infty = 0{\cdot}3$, $\alpha = 30^\circ$, $\mathrm{Re} = 1{\cdot}25\times10^6$, inboard position.

in cross-flow planes at the same chord stations, respectively. The tails cut through the vortex breakdown flow of the leading-edge vortex cores. The tail vortices are also outboard of the tails. The location of the vortex core with respect to the tail produces an increase in the aerodynamic damping, causing the tail deflections to decrease. The tail vortices are also shown to rotate in the opposite direction to those of the primary wing vortices. Figure 11 shows the spanwise distribution of the surface-pressure coefficient after 9·6 dimensionless time units from the initial conditions, covering the wing from $x = 0{\cdot}3$ to $x = 1{\cdot}0$. The suction peaks are less than those of the inboard twin-tail position.

Figure 12 shows the time history of bending and torsion deflections and load responses for the left and right tails for 20 dimensionless time units after the initial conditions. It is observed that the bending deflections are lower than those of the inboard twin-tail position, while the torsion deflections are substantially lower than those of the inboard twin-tail position. Moreover, both the bending and torsion deflections are out of phase of the normal force and twisting moment loads, in contrast with the case of inboard twin-tail position. The frequencies of the torsion deflections are almost twice those of the bending deflections, while the frequencies of the normal loads are almost the same as those of the twisting moments. However, the frequencies of the bending and torsion deflections are higher than those of the inboard twin-tail position.

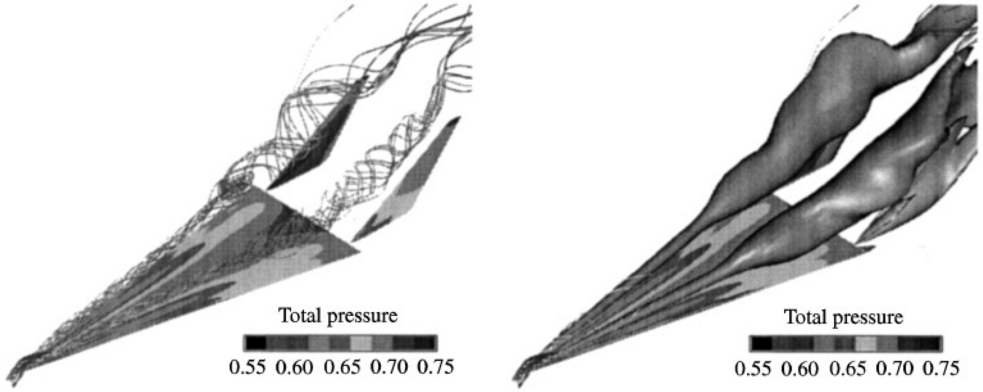

Figure 8. Three-dimensional views showing the total pressure on the surfaces, vortex core particle traces and iso-total pressure surfaces. Uncoupled case after $\tau = 9{\cdot}6$, outboard position.

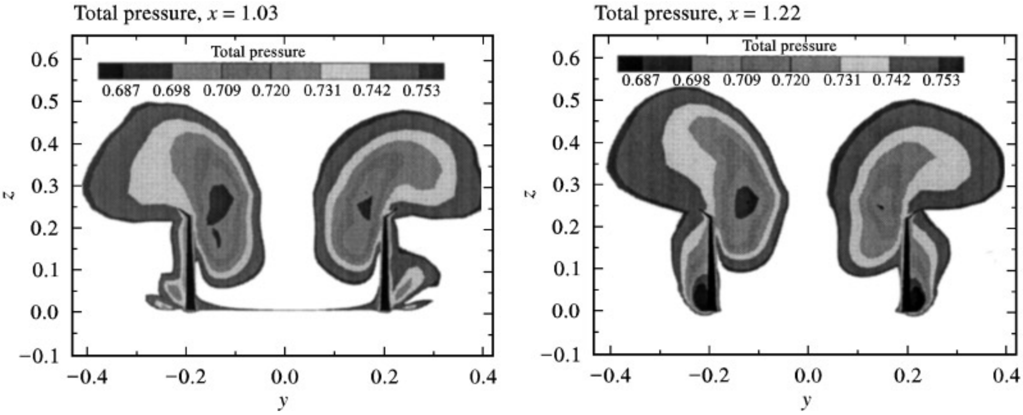

Figure 9. Snapshots of total pressure contours on cross-flow planes. Uncoupled case after $\tau = 9{\cdot}6$, outboard position.

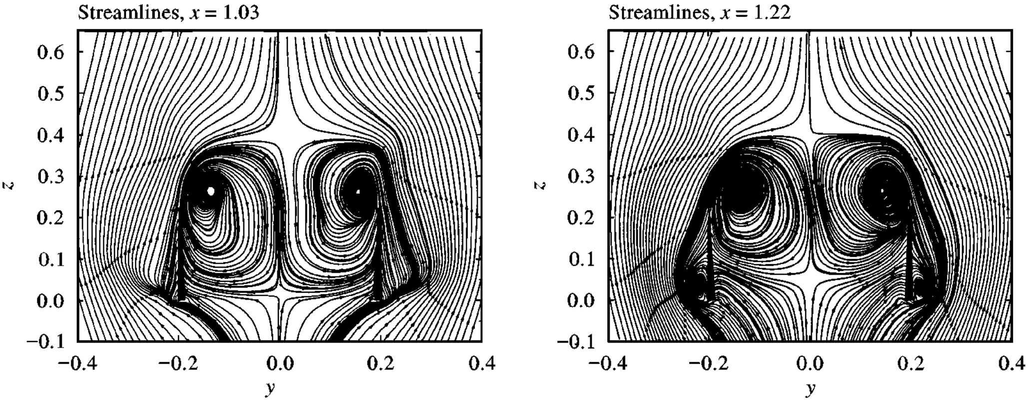

Figure 10. Snapshots of instantaneous streamlines on cross-flow planes. Uncoupled case after $\tau = 9{\cdot}6$, outboard position.

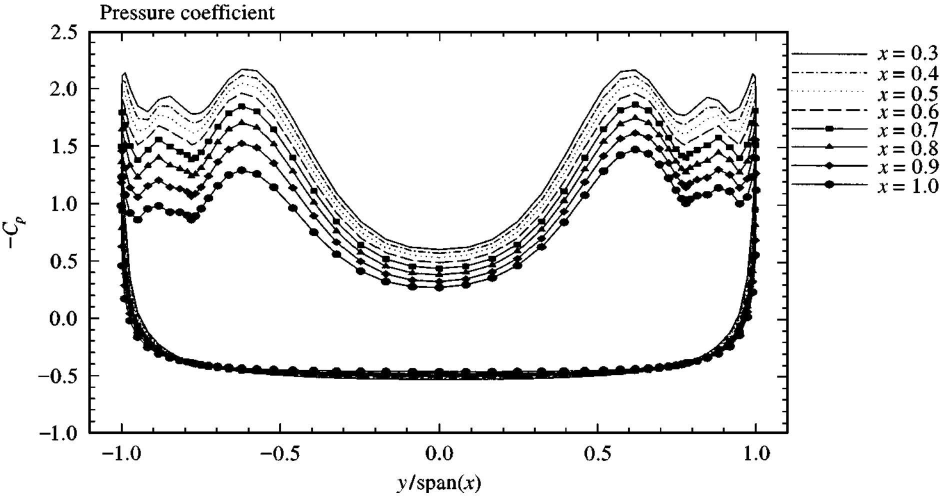

Figure 11. Distribution of pressure coefficient. Uncoupled case after $\tau = 9{\cdot}6$, outboard position.

Figure 13 shows the time history of the leading-edge total structural deflection and the root bending moment for the left and right tails for 20 dimensionless time units after the initial conditions. The levels of loads and deflections are much lower than those of the inboard twin-tail position. The tails are shown to oscillate in one direction only, in the first- and second-mode shapes.

4.3. COUPLED BENDING-TORSION MODES

Figures 14–20 show the results for the inboard position of the twin tail. Figure 14 shows three-dimensional views of the leading-edge vortex core particle traces and iso-total pressure surfaces. Figures 15 and 16 show front views of the total pressure contours on the wing surface and in cross-flow planes at $x = 1{\cdot}03$ and $x = 1{\cdot}22$, and the instantaneous streamlines in cross-flow planes at the same chord stations, respectively. Although, the vortex breakdown axial location is approximately at the same position as that of the uncoupled case, the shape and traces of the breakdown flow are different which show the upstream effect of the twin-tail motion. The vortex cores are moved more upward than those of the uncoupled case and continue moving upward as the flow travels downstream.

Figure 17 shows the spanwise distribution of the surface-pressure coefficient after 9·6 dimensionless time units from the initial conditions, covering the wing from $x = 0{\cdot}3$ to $x = 1{\cdot}0$.

Figures 18 and 19 show the time history of bending and torsion deflections and load responses for the left and right tails for 60 dimensionless time units after the initial conditions. The tail deflections and levels of loads are higher than those of the uncoupled case. However, the frequencies of the bending and torsion deflections, normal forces and twisting moments are the same as those of the uncoupled case. The normal forces are out of phase with the bending deflections, while the twisting moments are in phase with the torsion deflections.

Figure 20 shows the time history of the leading-edge total structural deflection and the root bending moment for the left and right tails for 60 dimensionless time units after the initial conditions. The tail deflections are in first-, second- and third-mode shapes. The two tails are moving opposite to each other in asymmetric manner.

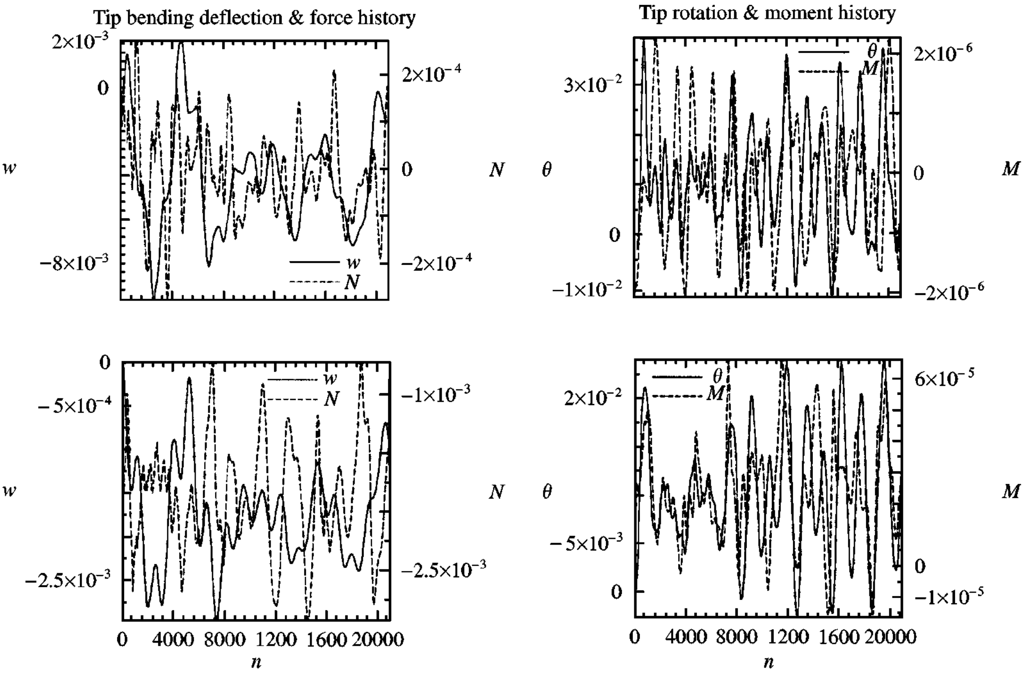

(a) Left tail

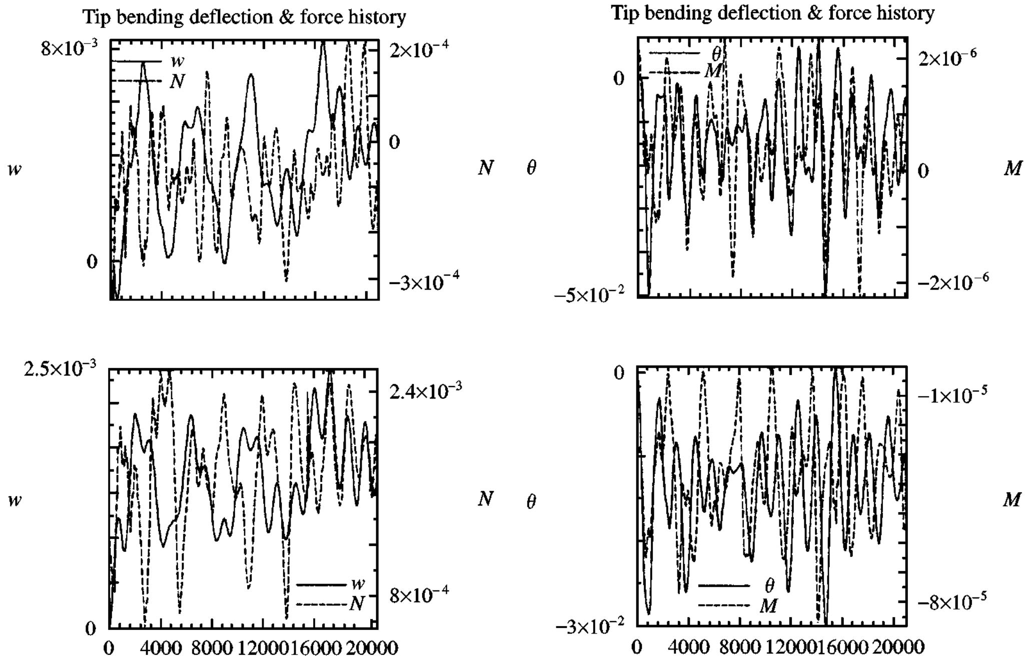

(b) Right tail

Figure 12. History of the deflection and load responses for an uncoupled bending-torsion case. $M_\infty = 0{\cdot}3$, $\alpha = 30^\circ$, $\mathrm{Re} = 1{\cdot}25 \times 10^6$, outboard position.

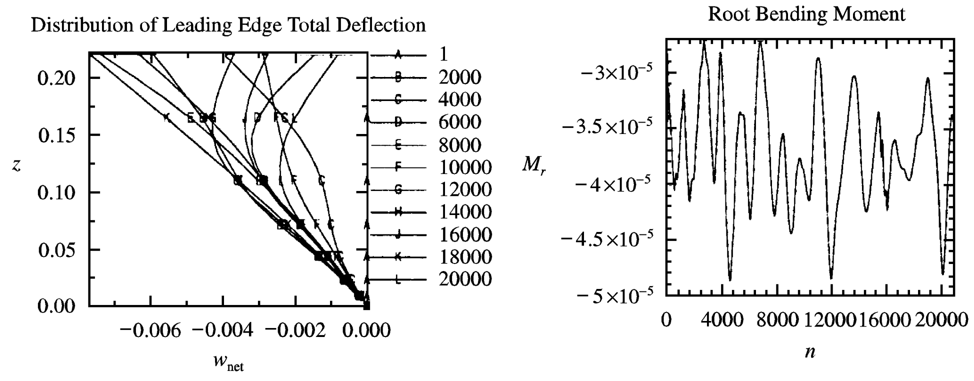

(a) Left tail

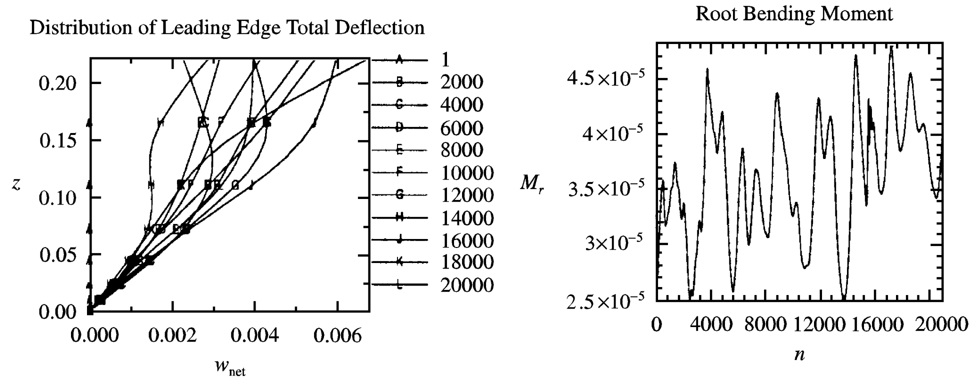

(b) Right tail

Figure 13. Tail leading-edge total structural deflections and root bending moment for an uncoupled bending-torsion case. $M_\infty = 0{\cdot}3$, $\alpha = 30°$, $\mathrm{Re} = 1{\cdot}25 \times 10^6$, outboard position.

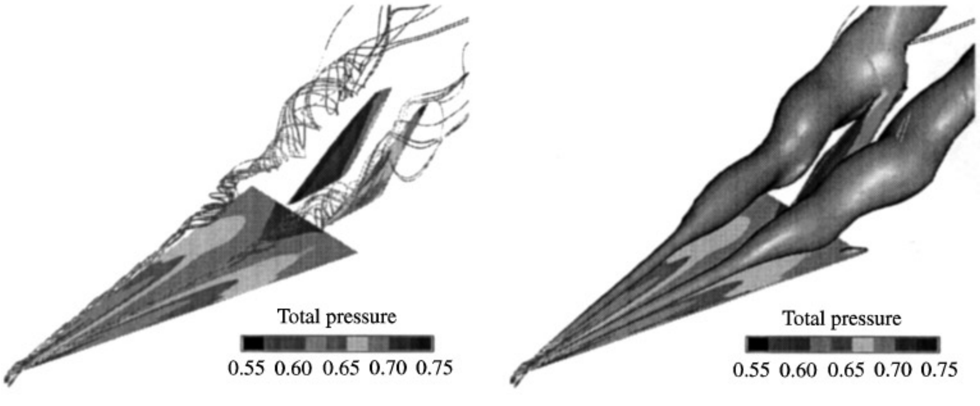

Figure 14. Three-dimensional views showing the total pressure on the surfaces, vortex core particle traces and iso-total pressure surfaces. Coupled case after $\tau = 9{\cdot}6$, $x_\theta = 0{\cdot}003$, inboard position.

Figures 21–27 show the results for the outboard position of the twin tail. Figure 21 shows three-dimensional views of the leading-edge vortex cores particle traces and iso-total pressure surfaces. Figures 22 and 23 show front views of the total pressure contours on the wing surface and in cross-flow planes at $x = 1{\cdot}03$ and $x = 1{\cdot}22$, and the instantaneous

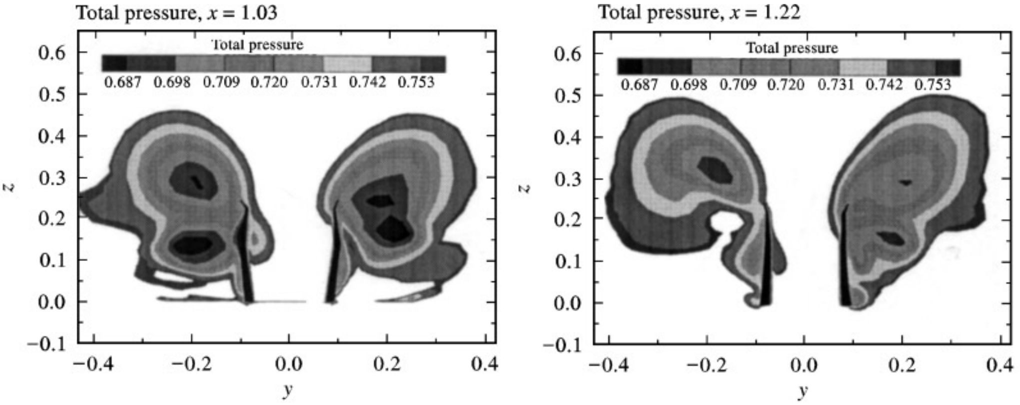

Figure 15. Snapshots of total pressure contours on cross-flow planes. Coupled case after $\tau = 9{\cdot}6$, $x_\theta = 0{\cdot}003$, inboard position.

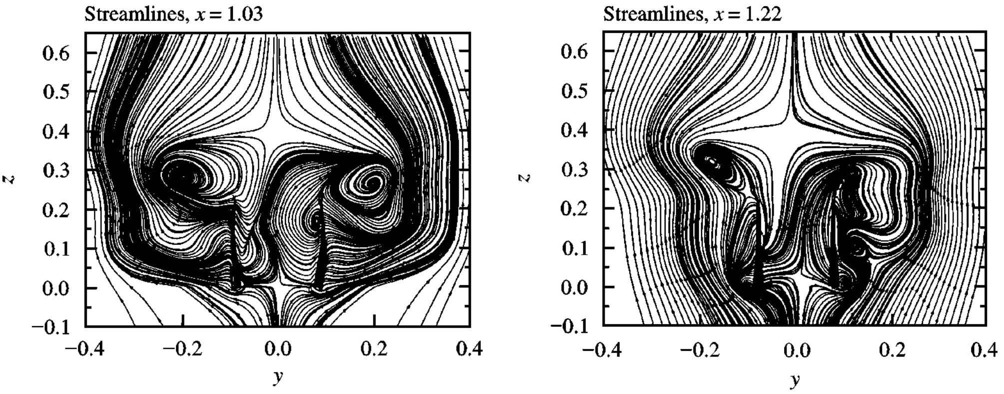

Figure 16. Snapshots of instantaneous streamlines on cross-flow planes. Coupled case after $\tau = 9{\cdot}6$, $x_\theta = 0{\cdot}003$, inboard position.

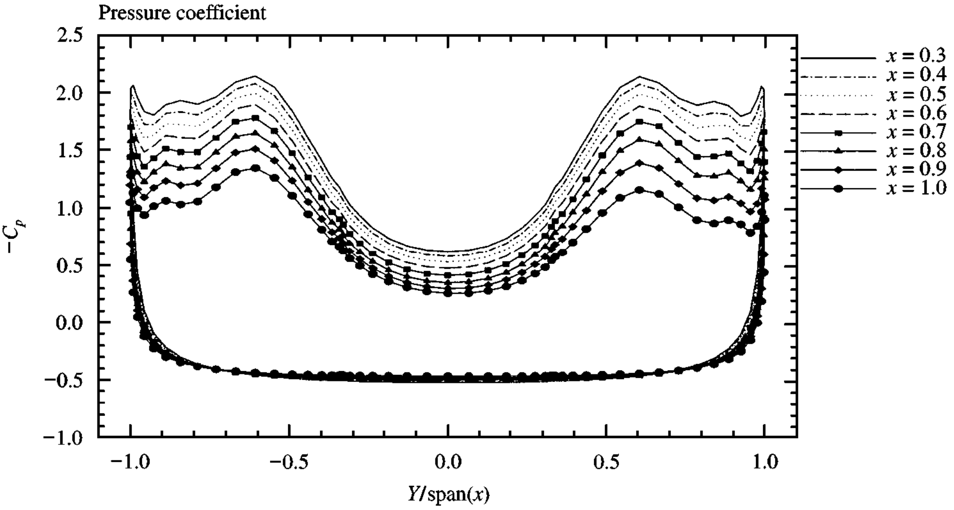

Figure 17. Distribution of the pressure coefficient. Coupled case after $\tau = 9{\cdot}6$, $x_\theta = 0{\cdot}003$, inboard position.

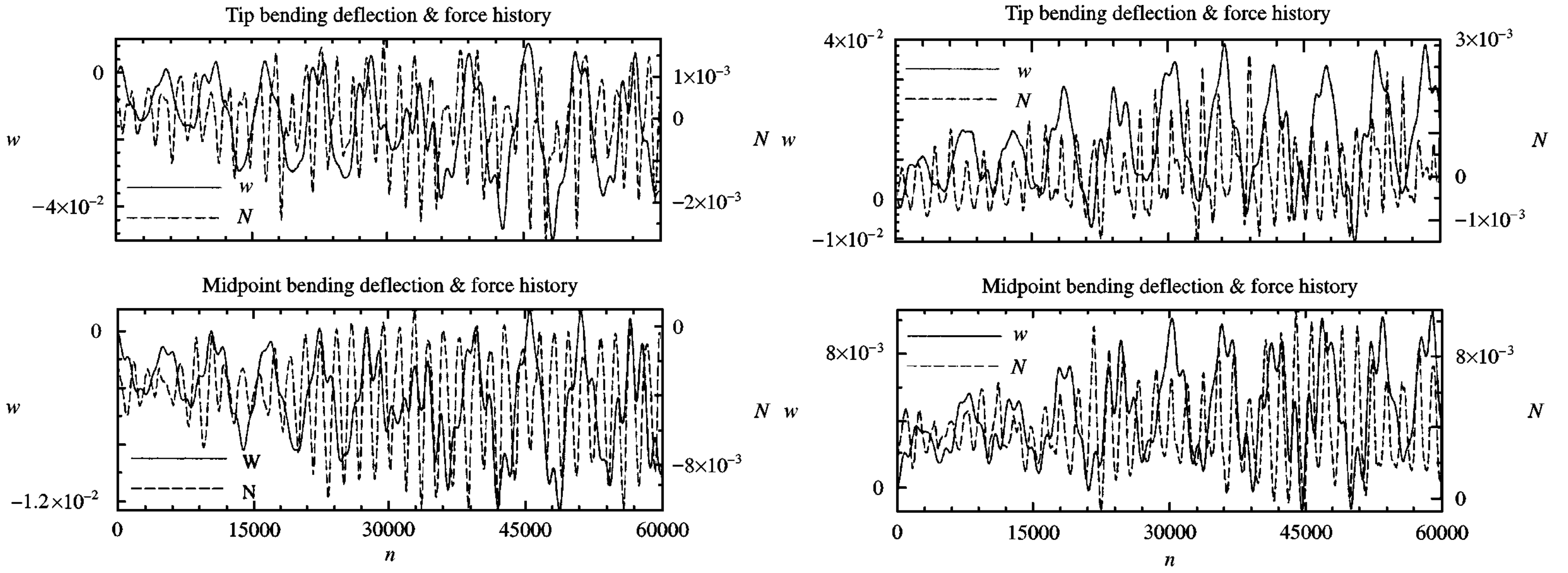

(a) Left tail

(b) Right tail

Figure 18. History of the bending deflection and load responses for coupled bending-torsion case, $x_\theta = 0{\cdot}003$. $M_\infty = 0{\cdot}3$, $\alpha = 30^\circ$, $\mathrm{Re} = 1{\cdot}25\times10^6$, inboard position.

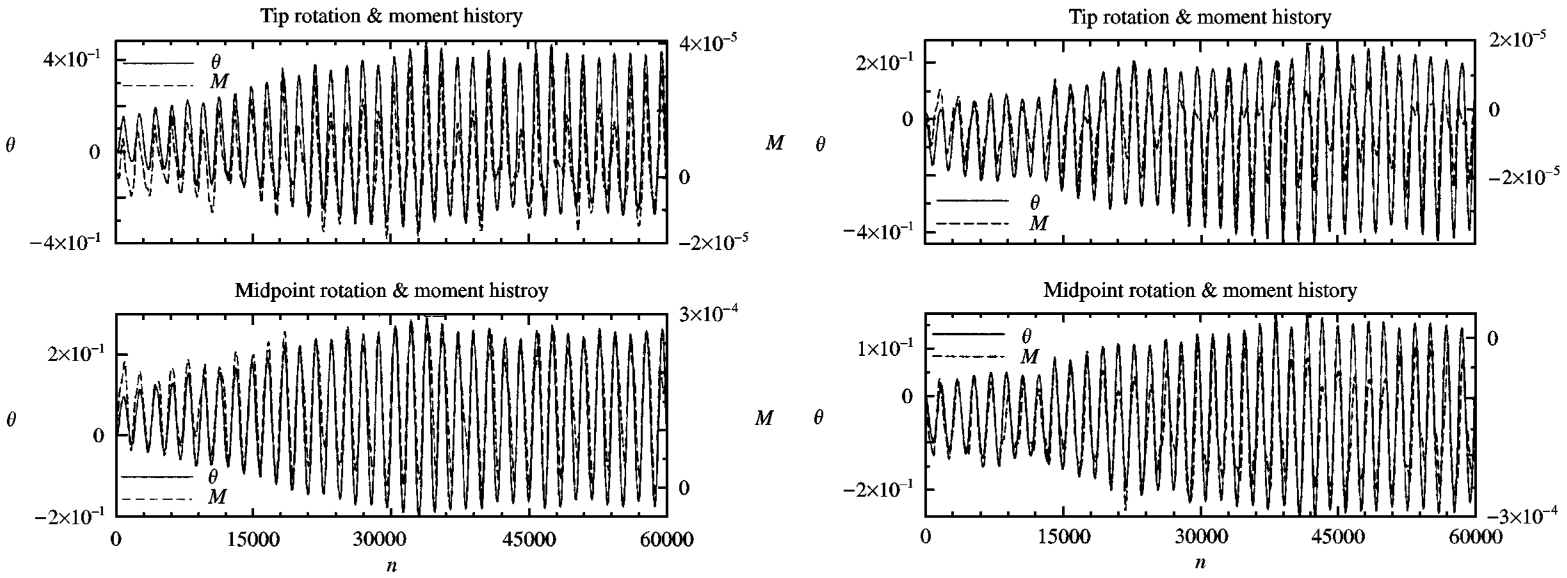

(a) Left tail

(b) Right tail

Figure 19. History of the torsion deflection and load responses for coupled bending-torsion case, $x_\theta = 0{\cdot}003$. $M_\infty = 0{\cdot}3$, $\alpha = 30^\circ$, $\mathrm{Re} = 1{\cdot}25 \times 10^6$, inboard position.

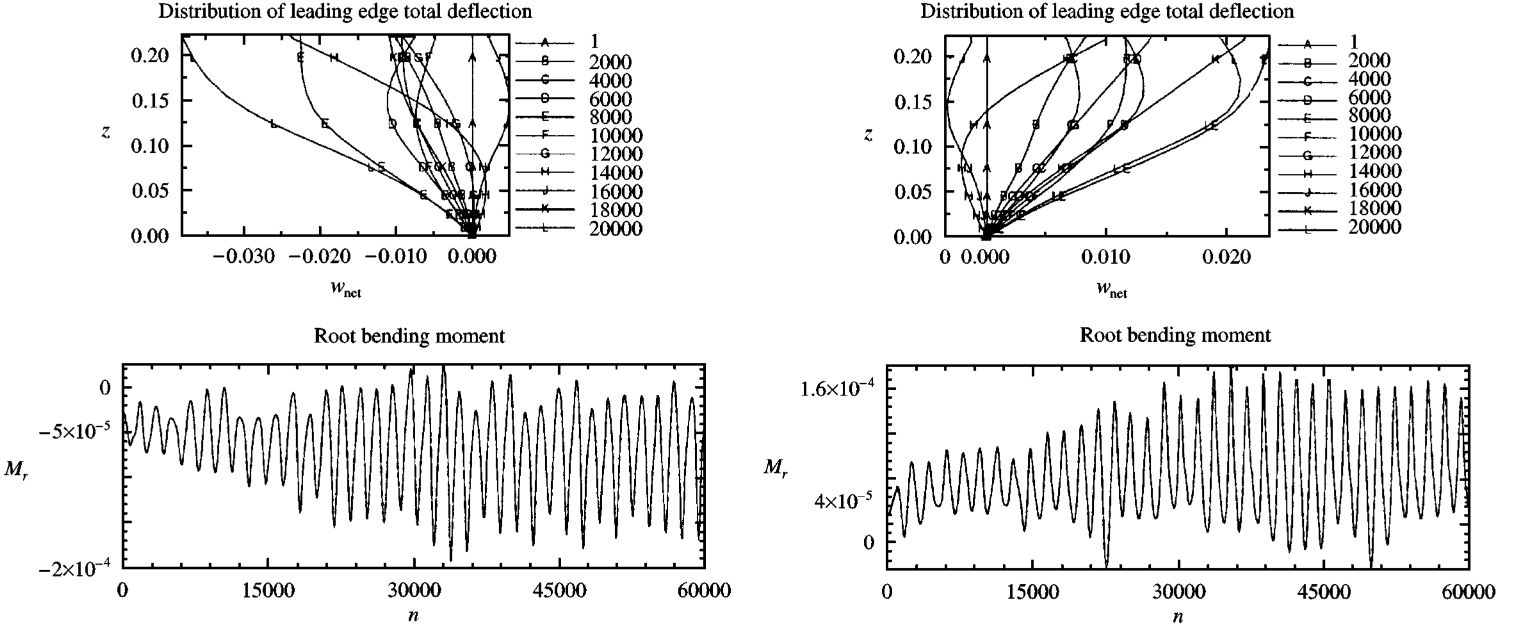

(a) Left tail

(b) Right tail

Figure 20. Tail leading-edge total structural deflections and root bending moment for coupled bending-torsion case, $x_\theta = 0{\cdot}003$. $M_\infty = 0{\cdot}3$, $\alpha = 30°$, $\mathrm{Re} = 1{\cdot}25 \times 10^6$, inboard position.

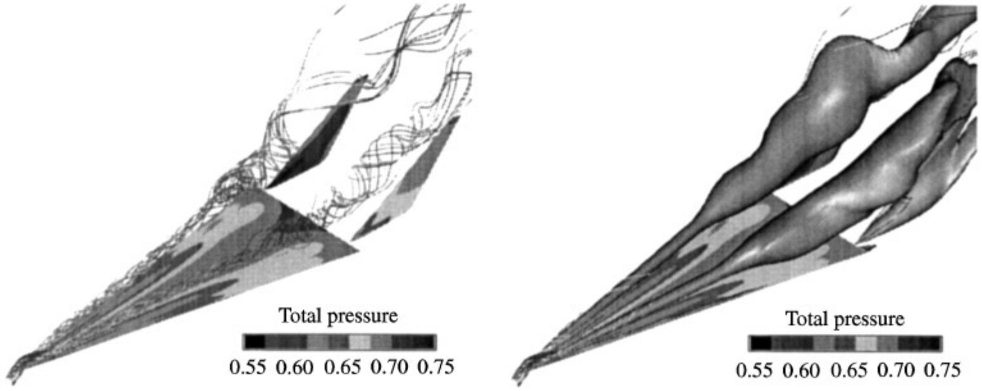

Figure 21. Three-dimensional views showing the total pressure on the surfaces, vortex core particle traces and iso-total pressure surfaces. Coupled case after $\tau = 9{\cdot}6$, $x_\theta = 0{\cdot}003$, outboard position.

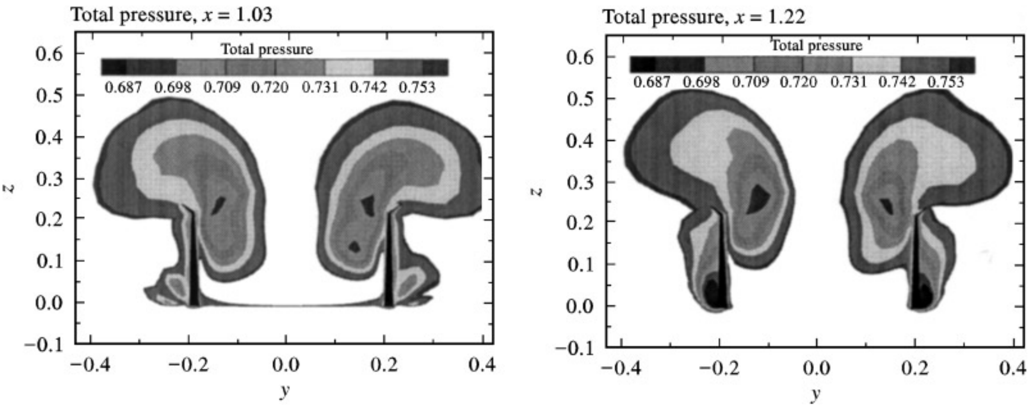

Figure 22. Snapshots of total pressure contours on cross-flow planes. Coupled case after $\tau = 9{\cdot}6$, $x_\theta = 0{\cdot}003$, outboard position.

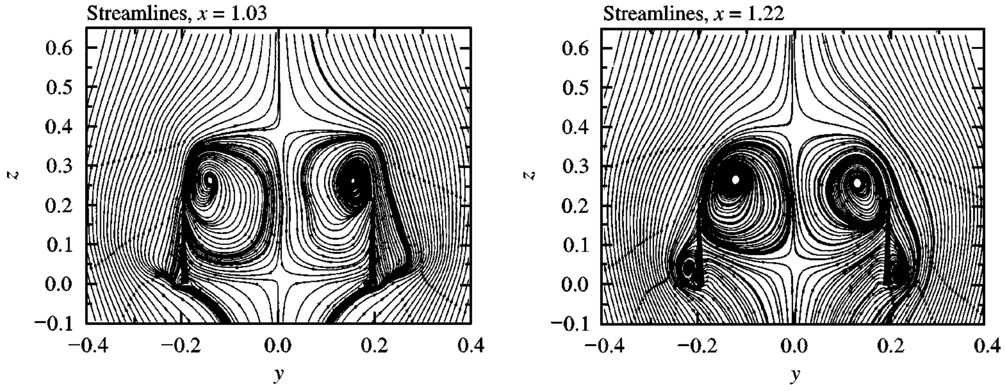

Figure 23. Snapshots of instantaneous streamlines on cross-flow planes. Coupled case after $\tau = 9{\cdot}6$, $x_\theta = 0{\cdot}003$, outboard position.

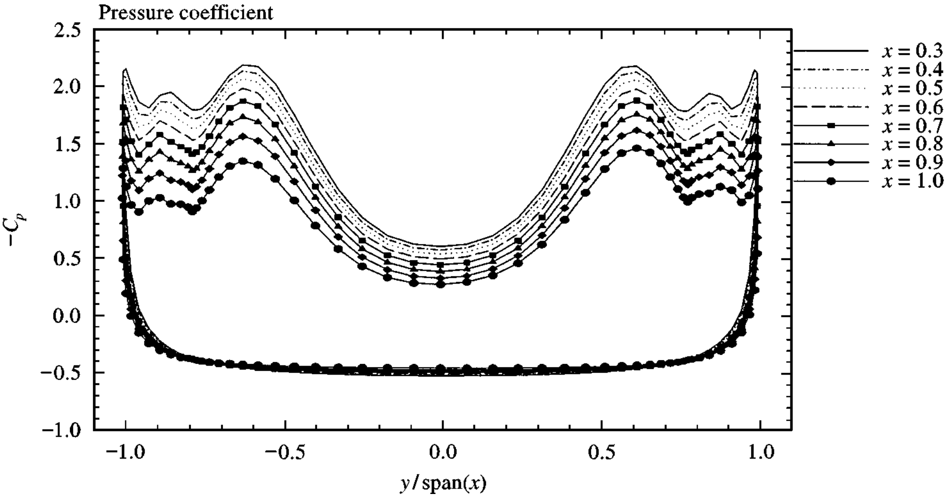

Figure 24. Distribution of coefficient of pressure. Coupled case after $\tau = 9{\cdot}6$, $x_0 = 0{\cdot}003$, outboard position.

streamlines in cross-flow planes at the same chord stations, respectively. The shape of the vortex breakdown is slightly different than that of the uncoupled case. This is because of the lower levels of the tail deflections which reduce the upstream effect on the flow.

Figure 24 shows the spanwise distribution of the surface pressure coefficient covering the wing from $x = 0{\cdot}3$ to $x = 1{\cdot}0$.

Figures 25 and 26 show the time history of bending and torsion deflections and load responses for the left and right tails for 60 dimensionless time units after the initial conditions. The tail deflections and levels of loads are higher than those of the uncoupled bending-torsion case of the outboard twin-tail position but still much lower than those of the uncoupled and coupled bending-torsion cases of the inboard twin-tail position. The bending and torsion deflections are out of phase of the normal force and twisting moment loads. The frequencies of the bending and torsion deflections are the same as those of the uncoupled bending-torsion case of the outboard twin-tail position but higher than those of the uncoupled and coupled bending-torsion cases of the inboard twin-tail position.

Figure 27 shows the time history of the leading-edge total structural deflection and the root bending moment for the left and right tails for 60 dimensionless time units after the initial conditions. The tails are deflected in one direction only in first- and second-mode shapes.

Table 1 shows the comparison of the present code (FTNS3D) results with those of Washburn *et al.* (1993) experimental data, of the mean root bending moment for flexible twin tails, the root-mean-square root bending moment for flexible twin tails and the lift coefficient with rigid twin tails. The computational results for both coupled and uncoupled bending and torsion modes agree well with Washburn's experimental data. The discrepancies in the results are attributed to the fact that the computational model has some differences from Washburn's experimental model. Our wing is a flat plate with zero thickness, while Washburn's wing is a Hummel-type wing (triangular cross-section). Although the tail shape is the same, our model assumed magnetically suspended solid material tails, while the Washburn tails are constructed with spars, additional ballast weights and void spaces in the tails. Our computational model assumed flexible twin-tail, while Washburn's experimental model involved one tail flexible and the other tail rigid. In the experimental work by Washburn *et al.* (1993), the presence of a flexible tail was found to affect the loads and pressures on the other rigid tail.

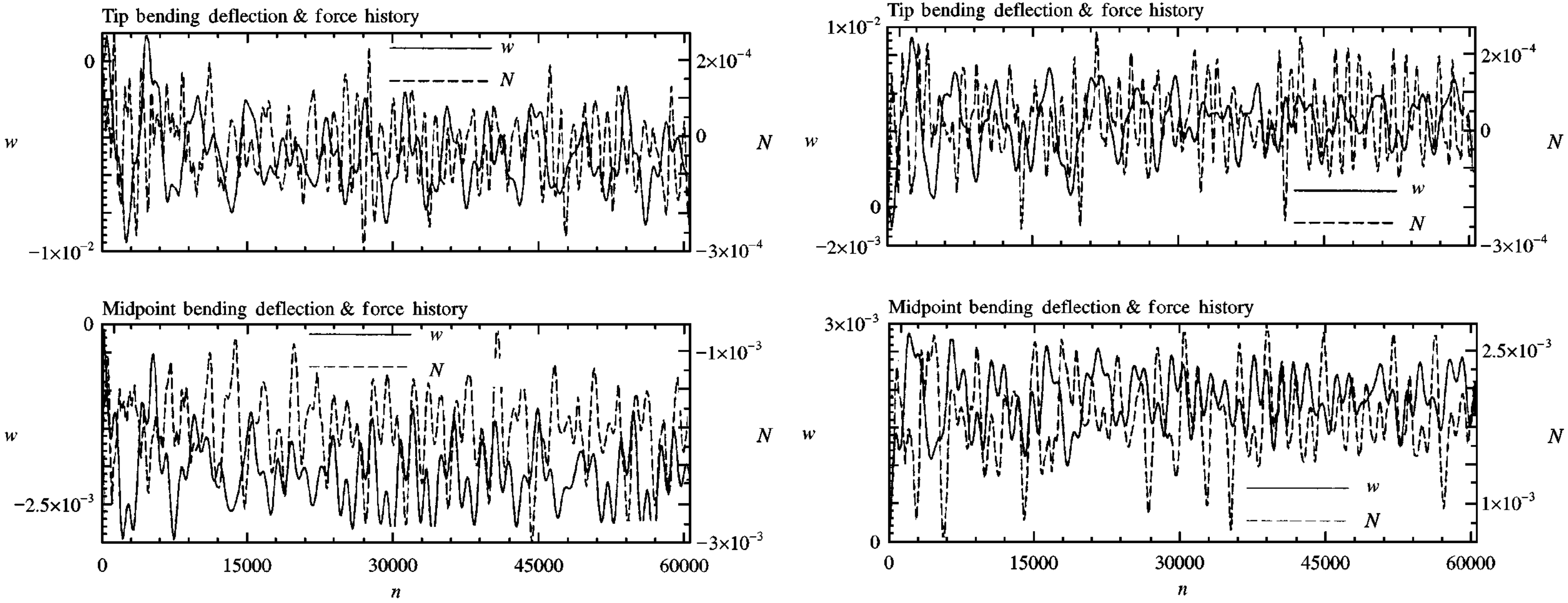

(a) Left tail

(b) Right tail

Figure 25. History of the bending deflection and load responses for coupled bending-torsion case, $x_0 = 0{\cdot}003$. $M_\infty = 0{\cdot}3$, $\alpha = 30°$, Re $= 1{\cdot}25 \times 10^6$, outboard position.

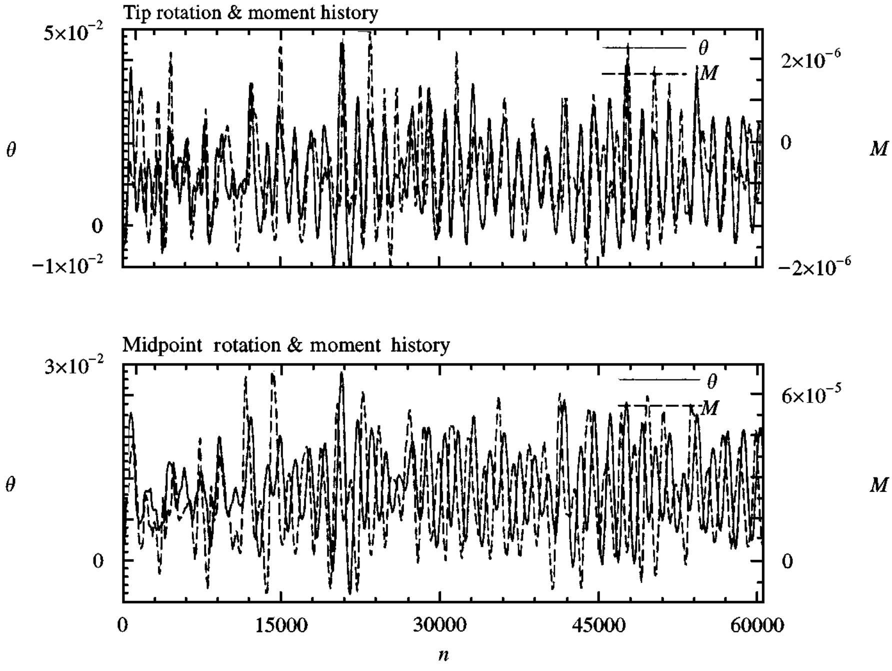

(a) Left tail

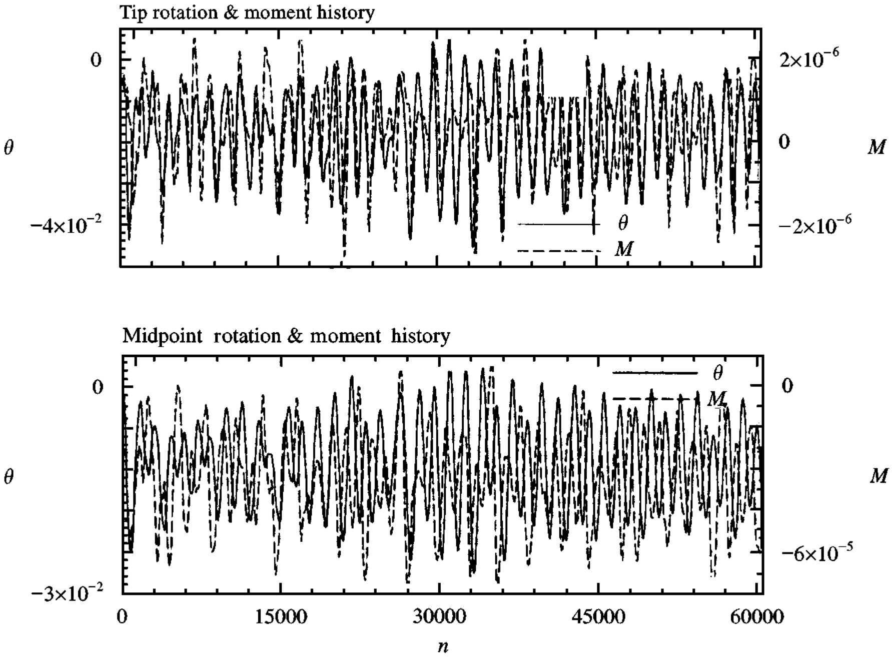

(b) Right tail

Figure 26. History of the torsion deflection and load responses for coupled bending-torsion case, $x_\theta = 0{\cdot}003$. $M_\infty = 0{\cdot}3$, $\alpha = 30°$, $\mathrm{Re} = 1{\cdot}25 \times 10^6$, outboard position.

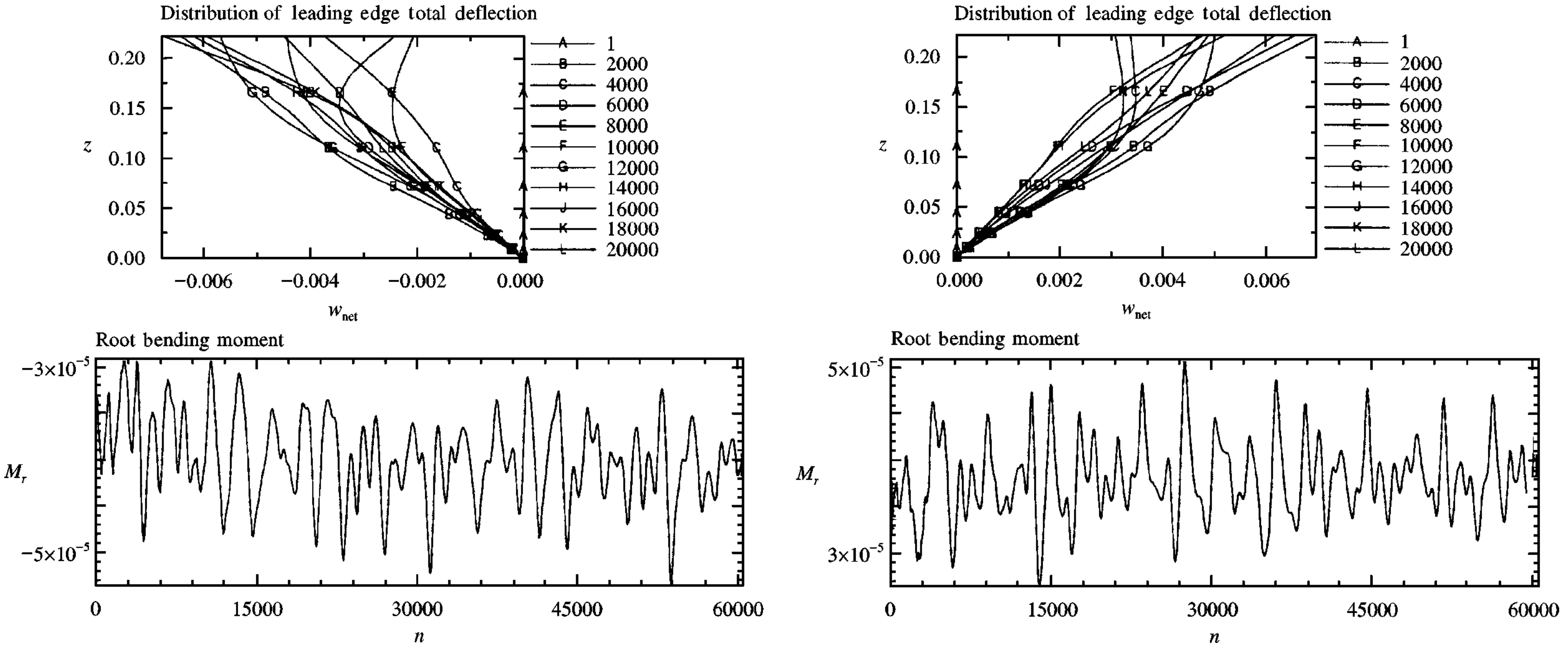

(a) **Left tail** (b) **Right tail**

Figure 27. Tail leading-edge total structural deflections and root bending moment for coupled bending-torsion case, $x_\theta = 0{\cdot}003$. $M_\infty = 0{\cdot}3$, $\alpha = 30^\circ$, Re $= 1{\cdot}25\times10^6$, outboard position.

TABLE 1

Validation of FTNS3D uncoupled and coupled computational results with Washburn *et al.* (1993) experimental data

Parameter	Position	FTNS3D uncoupled	FTNS3D coupled	WASHBURN
Mean-root bending moment	Inboard	0·1626	0·155	0·145
with flexible tails	Outboard	0·107	0·115	0·135
R.m.s. root bending moment	Inboard	0·042	0·064	0·024
with flexible tails	Outboard	0·011	0·01365	0·015
Lift coefficient	Inboard	1·0423	1·0411	1·10
with rigid tails	Outboard	1·07	1·055	1·10

5. CONCLUDING REMARKS

The effect of coupled and uncoupled bending and torsion modes on the twin-tail buffet response are investigated for different spanwise positions of the twin-tail. The coupled bending and torsion modes produce higher deflections and loads than those of the uncoupled mode cases. The inboard position of the twin-tail produces the largest bending and torsion loads and deflections when compared with the results of the outboard position. The frequencies of the bending and torsion loads and deflections in the case of outboard twin-tail position are higher than those of the inboard position. The frequencies of the torsion deflections are twice those of the bending deflections. It has been shown that the larger the tail deflections are, the higher the upstream effect is on the vortex breakdown flow upstream of the tails. The computational results presented are in good quantitative agreement with the experimental data of Washburn *et al.* (1993).

ACKNOWLEDGEMENT

This research work is supported under Grant No. NAG-1-648 and No. NAG-1-994 by the NASA Langley Research Center. The authors would like to recognize the computational resources provided by the NAS facilities at Ames Research Center and the NASA Langley Research Center.

REFERENCES

BEAN, D. E. & LEE, B. H. K. 1994 Correlation of wind tunnel and flight test data for F/A-18 vertical tail buffet. AIAA Paper 94-1800-CP.

COLE, S. R., MOSS, S. W. & DOGGET, R. V., Jr 1990 Some buffet response characteristics of a twin-vertical-tail configuration. NASA TM-102749.

ERICKSON, G. E., HALL, R. M., BANKS, D. W., DEL FRATE, J. H., SHREINER, J. A., HANLEY, R. J. & PULLEY, C. T. 1989 Experimental investigation of the F/A-18 vortex flows at subsonic through transonic speeds. AIAA Paper 89–2222.

KANDIL, O. A., KANDIL, H. A. & MASSEY, S. J. 1993 Simulation of tail buffet using delta wing-vertical tail configuration. AIAA Paper 93-3688-CP, *AIAA Atmospheric Flight Mechanics Conference*, Montery, CA, U.S.A., pp. 566–577.

KANDIL, O. A., MASSEY, S. J., & KANDIL, H. A., 1994 Computations of vortex-breakdown induced tail buffet undergoing bending and torsional vibrations. AIAA Paper 94-1428-CP, *AIAA/ASME/ASCE/ASC Structural, Structural Dynamics and Materials Conference*, Hilton Head SC, U.S.A. pp. 977–993.

Kandil, O. A., Massey, S. J. & Sheta, E. F., 1995 Structural dynamics/CFD interaction for computation of vertical tail buffet. *International Forum on Aeroelasticity and Structural Dynamics*, *Royal Aeronautical Society*, Manchester, U.K., 26–28 June, pp. 52.1–52.14. Also published in the *journal of the Royal Aeronautical Society*, August/September 1996, pp. 297–303.

Kandil, O. A., Sheta, E. F. & Liu, C. H., 1996 Computation and validation of fluid/structure twin-tail buffet response. *Euromech Colloquium 349*, Structure-Fluid Interaction in Aeronautics, Institut für Aeroelastik, Göttingen, Germany.

Kandil, O. A., Sheta, E. F. & Massey, S. J., 1997 Fluid/Structure twin tail buffet response over a wide range of angles of attack. AIAA Paper 97-2261-CP, *15th AIAA Applied Aerodynamics Conference*, Atlanta, GA, U.S.A.

Lee, B. & Brown, D., 1990 Wind tunnel studies of F/A-18 tail buffet. AIAA Paper 90–1432.

Sellers, W. L. III, Meyers, J. F. & Hepner, T. E., 1988 LDV survey over a fighter model at moderate to high angle of attack. SAE Paper 88–1448.

Washburn, A. E., Jenkins, L. N. & Ferman, M. A., 1993 Experimental investigation of vortex-fin interaction. AIAA Paper 93-0050, Reno, NV, U.S.A.

Wentz, W. H., 1987 Vortex-Fin interaction on a fighter aircraft. AIAA Paper 87-2474, *AIAA Fifth Applied Aerodynamics Conference*, Monterey, CA, U.S.A.